Global distribution pattern in characteristics of gross primary productivity response to soil water availability

Shanning Bao[1*], Nuno Carvalhais[2,3,4], Jian Xu[1], Jingming Chen[5,6], Yang Lei[1], Gegen Tana[1], Changgui Lin[1], Jiancheng Shi[1]

1. National Space Science Center, Chinese Academy of Sciences, 100190, Beijing, China

2. Department for Biogeochemical Integration, Max-Planck-Institute for Biogeochemistry, 07745, Jena, Germany

3. Departamento de Ciências e Engenharia do Ambiente, DCEA, Faculdade de Ciências e Tecnologia, FCT, Universidade Nova de Lisboa, 2829-516 Caparica, Portugal

4. ELLIS Unit Jena, 07745, Jena, Germany

5. School of Geographical Science, Key Laboratory for Humid Subtropical Eco-Geographical Processes of the Ministry of Education, Fujian Normal University, Fuzhou 350008, China

6. Department of Geography and Planning, University of Toronto, 100 St. George St., Toronto, Ontario M5S3G3, Canada

*Corresponding author: Shanning Bao, baoshanning@nssc.ac.cn

Abstract: Water stress is a main factor limiting the vegetation carbon assimilation rate, especially in semi-arid and arid regions. This study aims to analyze the characteristics of GPP response to soil water availability by three parameters, W_I, k_W and a_W, based on a light-use-efficiency (LUE) model. These parameters describe the inflection point, slope and lag effect of GPP response to soil water availability changes, respectively, reflecting the average water constraints, responding speed to soil water variations and degree of lagged effect. We utilized a hybrid approach by coupling machine learning techniques with the LUE model to learn intricate relationships between these parameters and features encompassing climate, vegetation, nutrient deposition, soil properties and elevation across 196 eddy covariance sites. The results showed that the spatial variability of these three parameters was dominated by plant types, enhanced vegetation index (EVI) variability, forest age, soil properties,

25 and bioclimatic conditions. Mixed and deciduous broadleaf forests alongside vegetation characterized by lower

26 temporal EVI variability and older forests (>50 years) displayed statistically lower W_I and k_W, indicating

27 generally fewer water limitations and quicker responses to changes in soil water availability, in contrast to shrubs

28 and grass. The impact of soil properties on the spatial distribution of water sensitivities was significant but

29 complex. Rising temperatures can intensify the average water limitation and reduce the response speed to soil

30 water changes. The spatial distribution patterns of W_I and k_W generally followed the climate aridity. Vegetation

31 in most arid regions exhibited lagged responses to soil water availability. Uncertainties in W_I and k_W were higher

32 in the tropics due to limited datasets and in humid areas due to neural network structures, underscoring the

33 importance of training datasets and approaches in GPP sensitivity analysis. Our study highlights the spatial

34 heterogeneity of carbon assimilation responses to climate changes driven by diverse vegetation, climate and soil

35 properties.

36 **Keywords**: gross primary productivity, water sensitivity, response curve feature, spatial distribution, lag effect,

37 hybrid model

1. Introduction

39 Soil water availability is one of the primary factors influencing the temporal variability in carbon assimilation

40 rates[1, 2]. Water limitations are reported to have an increasing impact on ecosystem productivity, especially

41 gross primary productivity (GPP) [3]. Despite various studies exploring the spatial distribution pattern of soil

42 water sensitivity using different photosynthesis models[1, 2, 4, 5], the specifics of the GPP response to water

43 availability changes remain unclear, such as the inflection point, slope and lagged effect of the GPP response.

44 Investigating the spatial patterns of GPP response to water availability is essential for forecasting carbon uptake

45 trends in our aridity-changing world[6, 7].

46 In photosynthesis models, GPP responses to water stress are described and controlled by several model

47 parameters, which are typically assigned according to plant functional types (PFTs) or set as fixed values in

48 traditional photosynthesis models. For example, the first proposed MODIS global gross primary productivity

49 (GPP) product based on a light use efficiency (LUE) model applied a PFT-based look-up table for the parameters

50 controlling responses of GPP to absorbed light, temperature and vapour pressure deficit (VPD)[8]. The optimal

51 soil water availability (also known as inflection point or soil moisture threshold) in LUE models was usually set

52 based on PFT or fixed values [9, 10]. Moreover, PFT-based parameterization is widely used in photosynthesis

53 models stemming from the FvCB leaf-scale photosynthesis process model[11]. A representative case is the

54 photosynthesis module in the community land model (CLM) series[12]. It adopts the PFT-based

55 parameterization approach for the specific leaf area and leaf nitrogen for carboxylation, while fixing water-

56 stress-related parameters globally. Other kinds of dynamic global vegetation models (DGVMs) in TRENDY and

57 global climate models in the CMIP6 ensemble are also parameterized according to PFT[13, 14]. In general, the

58 parameter variability within PFT is ignored in traditional photosynthesis models, resulting in poor simulations

59 in many cases and high uncertainties[15].

60 The water response function parameters in photosynthesis models can be calibrated locally according to the

61 observational carbon flux data available at hundreds of eddy covariance sites (e.g., FLUXNET). Many models,

62 such as CASA, PRELES, EC-LUE, and TL-LUE parameters, were optimized and improved through site

63 calibrations[16-19], reflecting notable parameter variability beyond PFT. However, model parameters cannot be

64 calibrated per grid at the global scale due to the limited number of EC sites. Many studies chose to extrapolate

65 parameters according to PFT[18], site-similarity[16] or applied unified parameters[20]. The PFT-based

66 extrapolation approach assumes that photosynthesis model parameters vary with PFT only, neglecting other

67 possible dominating factors, e.g., climate and soil properties which are related to photosynthesis sensitivities.

68 The links between photosynthesis model parameters and ecosystem properties, including vegetation and climatic

69 characteristics, were demonstrated independently[21-23]. These studies illustrated that the variability of

70 photosynthesis model parameters, representing the photosynthesis sensitivities, can be explained by vegetation

71 and climate features. Existing literature does not directly reveal drivers and distribution patterns of water

72 sensitivity parameters, while highlighting the importance of root-zone water storage capacity for GPP

73 responses[24] and the complexity of the vegetation sensitivities to soil moisture[4]. In light of these facts, Horn

74 et al[25] and Peaucelle et al[26] predicted photosynthesis model parameters using plant traits and climate

75 features to improve model extrapolation ability. However, these studies based on calibrated parameters were

76 restricted from parameter equifinality and unable to detect the actual relationship between parameters and

77 ecosystem properties.

78 Hybrid models coupling traditional process models with machine learning techniques enable the exploration of

79 parameter variability. Bao et al.[27] proposed a simultaneous model parameter inversion and extrapolation (SPIE)

80 approach which can parametrize an LUE model based on ecosystem properties. The approach embeds the

81 traditional LUE model into a neural network structure, which can output GPP and model parameters

82 simultaneously. With the approach, the variability and distribution patterns of the parameters determining GPP

83 responses to soil water availability can be learned.

84 This study focuses on the analysis of variability and distribution patterns of the GPP sensitivity to water stress.

85 We took advantage of three parameters in a LUE model to represent the average soil water limitation, soil water

86 responding speed and lagged responses of GPP to water stress. The three parameters describe the inflection

87 point, the slope and lag effect of the soil water response function of GPP in the LUE model. We applied SPIE to

88 learn the relationship between these parameters and features denoting vegetation, climate, atmospheric nutrient

89 deposition, terrain and soil properties. The learned relationship was used to extrapolate the parameters and

90 explore their spatial variability. Our study can contribute to a better understanding of the link between ecosystem

91 features and the water sensitivity of carbon assimilation rates and offers global distribution maps of these water

92 sensitivity parameters.

93 **2. Data and Methods**

94 2.1   Light use efficiency model

95 The LUE model is selected from a large ensemble of models with various combinations of environmental drivers

96 and sensitivity functions[28]. It is evaluated against observations across different site groups and plant-climate

97 types at daily, weekly, monthly and annual scales, and the results show that the model significantly outperforms

98 other models. The model has a typical LUE structure which defines GPP as the product of maximum light use

99 efficiency (ε_{max}), absorbed photosynthetically active radiation (APAR) and the environmental sensitivity

100 functions. APAR is the product of the incoming photosynthetically active radiation (PAR) and the fraction of

101 the absorbed photosynthetically active radiation (FAPAR). The environmental sensitivity functions represent

102 the environmental impacts on the photosynthesis process, including sensitivity functions of air temperature (T),

103 vapour pressure deficit (VPD), atmospheric CO_2 concentration (C_a), soil water availability (W), light intensity

104 (L) and cloudiness index (CI). fC_a represents the fertilization effect of CO_2, while the other sensitivity functions

105 all represent the environmental stress downregulating GPP, i.e., making GPP smaller than the potential GPP

106 under optimal T, VPD, W, APAR and fully diffused radiation. The model equation is as follows:

107
$$\text{GPP} = \varepsilon_{max} \cdot \text{APAR} \cdot f\text{T} \cdot f\text{VPD} \cdot fC_a \cdot f\text{W} \cdot f\text{L} \cdot f\text{CI} \qquad\qquad 1$$

108 All sensitivity functions range from zero to one except fC_a (≥ 1). The fL and fCI can be also used to represent the

109 limitation from light saturation and the fertilization from diffuse radiation, respectively. The detailed equations

110 of the sensitivity functions are listed at eq. 2-7.

111
$$f\text{T} = \frac{2e^{-(T_f - T_{opt})/k_T}}{1 + e^{(-(T_f - T_{opt})/k_T)^2}} \qquad\qquad 2$$

112
$$f\text{VPD} = e^{\kappa\left(\frac{C_{a0}}{C_a}\right)^{C_K}\text{VPD}} \qquad\qquad 3$$

113
$$fC_a = 1 + \frac{C_a - C_{a0}}{C_a - C_{a0} + C_m} \qquad\qquad 4$$

114
$$f\text{W} = \frac{1}{1 + e^{k_W(w_f - W_I)}} \qquad\qquad 5$$

115
$$f\text{L} = \frac{1}{1 + \gamma \cdot \text{APAR}} \qquad\qquad 6$$

116
$$f\text{CI} = \text{CI}^{\mu} \qquad\qquad 7$$

117
$$T_f(t) = (1 - \alpha_T) \cdot T(t) + \alpha_T \cdot T_f(t - 1) \qquad\qquad 8$$

118
$$W_f(t) = (1 - \alpha_W) \cdot W(t) + \alpha_W \cdot W_f(t - 1) \qquad\qquad 9$$

119 The LUE model parameters (in **bold** and *italic*) indicate the sensitivities of GPP. *t* refers to the time step.

120 Equations **Error! Reference source not found.-Error! Reference source not found.** are the lag functions for

121 GPP responses to temperature and soil moisture in boreal climates and arid climates, respectively. The units and

122 ranges of these parameters are listed in Table S1.

123 The water sensitivity parameters refer to W_I, k_W and α_W, which are the inflection point, slope of water response

124 function and the lagged effect of soil water availability changes in arid climates (see how the soil water sensitivity

125 of GPP, fW, vary with the three parameters in Figure 1). W_I indicates the average water limitation on GPP and

126   k_W reflects the responding speed of GPP to W changes. The combination of a low W_I and a low k_W (=high

127   absolute value) implies that GPP is impacted by soil moisture only below a relatively lower threshold while

128   decreasing rapidly due to water limitation. α_W closing to one represents the lagged response of GPP to W due to

129   the green tissue development in the vegetation after drought. Therefore, we use these three parameters to

130   diagnose the average soil water limitation, responding speed and lagged responses of GPP.
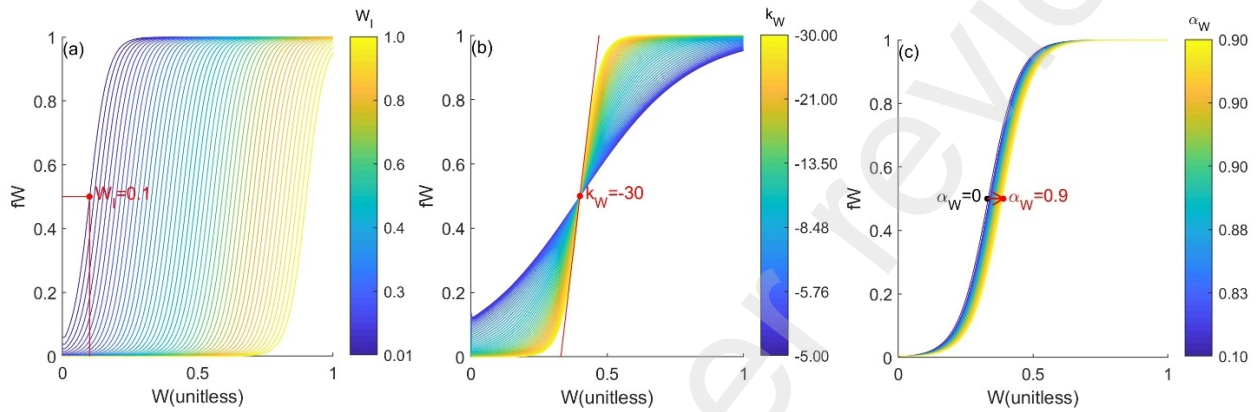
131

132   **Figure 1. The sensitivity function of GPP to W (fW) changes with three water sensitivity parameters**
133   **(W_I, k_W and α_W). W_I represents the inflection point of the fW, which is equal to the W resulting in fW=0.5**
134   **(exemplified as the red point shown in Figure1a); k_W is the slope of the fW; α_W represents the degree of**
135   **the lag effect, i.e., the GPP response to W changes is lagged when α_W is close to 0.9 and the GPP response**
136   **is instantaneous when α_W is close to zero.**

137   2.2   Forcing data

138   The forcing data for the LUE model is collected at 196 EC sites from FLUXNET (https://fluxnet.org/). The data

139   from EC sites include daily global radiation (R_g, MJ·m^{-2}·d^{-1}), T (°C), VPD (hPa), precipitation (Precip, mm),

140   potential evapotranspiration (PET, mm), potential radiation (MJ·m^{-2}·d^{-1}), and latent heat (LE, W·m^{-2}). PAR is

141   estimated by R_g and 0.45 (denotes the fraction of visible bands). The water availability index (WAI, mm) is

142   calculated using PET and Precip with two parameters, the maximum available soil water content (AWC) and ET

143   decay coefficient (θ), as shown in 10-12[29, 30]. We normalized the WAI using equation 13 to calculate the W

144   representing the relative soil water availability. W serves as an input for the LUE model.

145        $$minP = min(Precip(t), AWC - WAI(t-1)) \tag{10}$$

146        $$ET_{sim}(t) = min(PET(t), \theta \cdot (WAI(t-1) + minP)) \tag{11}$$

147        $$WAI(t) = WAI(t-1) - ET_{sim}(t) + minP \tag{12}$$

148           $W = WAI/AWC$

149 Here, ET and WAI can be both estimated using Precip and PET. AWC and θ are predicted together with the

150 LUE model parameters. Snow sublimation is considered according to Trautmann et al[30]. Before estimation,

151 all state variables are initialized by at least a 5-year spin-up period.

152 CI is equal to one minus the global radiation by the potential radiation, which is linearly correlated to the fraction

153 of diffuse radiation to the global radiation. The daily evapotranspiration (ET, mm) is estimated based on LE and

154 T and used to optimize WAI parameters.

155 We adopt normalized difference vegetation index (NDVI) to represent FAPAR for their linear relationship. The

156 NDVI is calculated using the red and near-infrared bands of MODIS directional hemispherical reflectance

157 product at the resolution of 500m (MCD43A3), averaging from the nearest four pixels. The gaps in temporal

158 NDVI at each site are filled with the FluxnetEO dataset[31]. The monthly mean atmospheric CO_2 concentration

159 (ppm) is acquired from the NOAA website (https://www.esrl.noaa.gov/gmd/) and linearly interpolated to the

160 daily scale.

161 We collect the GPP and ET estimated from the observational net ecosystem exchange and latent heat flux

162 (hereafter referred to as GPP_{obs} and ET_{obs}) and the relative uncertainties. These data are used to optimize the

163 neural network and validate the simulated GPP and ET (hereafter referred to as GPP_{sim} and ET_{sim})

164 2.3 Model inputs

165 The model inputs for parameter determination include PFT, bioclimatic variables (BIO1-19), aridity index (AI1-

166 2), vegetation index features (VIF1-8), forest age, atmospheric nutrient deposition, soil properties and elevation

167 (Table 1). At the site level, PFT and elevation are collected from the site information on the FLUXNET website.

168 The 19 bioclimatic variables and aridity index are calculated based on the WorldClim global meteorological

169 product from 1970-2000 with a 1km resolution[32, 33]. The vegetation index features are calculated based on

170 the enhanced vegetation index (EVI, multiplied by 100), which was computed using the red, near-infrared and

171 blue bands of Landsat 5, 7 and 8 from 1986-2015 (downloaded via Google Earth Engine) around each site with

172 a window size of 1km. The forest age is extracted from the global forest age product at 1km resolution which is

173 estimated based on inventories, biomass and climate data[34]. The ages of cropland and grassland are set to be

174 zero. The atmospheric nitrogen and phosphorus deposition datasets were extracted from the nearest pixel of the

175 modelled global nutrient deposition product from 1986-2015[35]. Moreover, we collect 16 soil property

176 variables for the surface soil layer at each site from the mean of the nearest pixels of SoilGrids[36] within a

177 window of 1km.

178

Table 1. Definition of input features

Class	Short names	Definitions
Categorical variable/PFT	CRO	Croplands
	CSH	Closed shrublands
	DBF	Deciduous broadleaf forests
	EBF	Evergreen broadleaf forests
	ENF	Evergreen needleleaf forests
	GRA	Grasslands
	MF	Mixed forests
	OSH	Open shrublands
	SAV	Savannas
	WET	Wetlands
	WSA	Woody savannas
Bioclimatic variables	BIO1	Annual mean temperature in °C
	BIO2	Mean diurnal range in °C (mean of monthly maximum temperature minus minimum temperature)
	BIO3	Isothermality (BIO2 divided by BIO7 and 100)
	BIO4	temperature seasonality in 10^2°C (standard deviation of temperature multiplied by 100)
	BIO5	Max temperature of warmest month in °C
	BIO6	Min temperature of coldest month in °C
	BIO7	Temperature annual range in °C (BIO5 minus BIO6)
	BIO8	Mean temperature of wettest quarter in °C
	BIO9	Mean temperature of driest quarter in °C
	BIO10	Mean temperature of warmest quarter in °C
	BIO11	Mean temperature of coldest quarter in °C
	BIO12	Annual precipitation in mm
	BIO13	Precipitation of wettest month in mm
	BIO14	Precipitation of driest month in mm
	BIO15	Precipitation seasonality (coefficient of variation)
	BIO16	Precipitation of wettest quarter in mm
	BIO17	Precipitation of driest quarter in mm

	BIO18	Precipitation of warmest quarter in mm
	BIO19	Precipitation of coldest quarter in mm
Aridity features	AI1	Mean annual aridity index (ratio between mean annual precipitation and potential evapotranspiration)
	AI2	seasonality of aridity index (standard deviation of mean monthly aridity index)
Vegetation features	VIF1	Annual mean EVI
	VIF2	EVI seasonality (standard deviation of monthly EVI relative to the mean EVI)
	VIF3	Max EVI of warmest month
	VIF4	Min EVI of coldest month
	VIF5	Mean EVI of wettest quarter
	VIF6	Mean EVI of driest quarter
	VIF7	Mean EVI of warmest quarter
	VIF8	Mean EVI of coldest quarter
	Age	Forest age (in years)
Atmospheric nutrient deposition	Ndep$_{NHX}$	Average atmospheric nitrogen deposition (NH_3 and NH_4)
	Ndep$_{NOY}$	Average atmospheric nitrogen deposition (NO and NO_2)
	Pdep	Average atmospheric phosphorus deposition
Soil properties	BDRLOG	Probability of occurrence (0-100%) of R horizon
	BDTICM	Absolute depth to bedrock (in cm)
	BLDFIE	Bulk density (fine earth) in kg/m^3
	CECSOL	Cation exchange capacity of soil in cmol/kg
	CLYPPT	Clay content (0-2 mm) mass fraction in %
	CRFVOL	Coarse fragments volumetric in %
	ORCDRC	Soil organic carbon content (fine earth fraction) in g/kg
	PHIHOX	Soil pH*10 in H_2O
	PHIKCL	Soil PH*10 in KCl
	SLTPPT	Silt content (2-50 mm) mass fraction in %
	SNDPPT	Sand content (50-2000 mm) mass fraction in %
	AWCh1	Derived available soil water capacity (volumetric fraction) with FC = pF 2.0
	AWCh2	Derived available soil water capacity (volumetric fraction) with FC = pF 2.3
	AWCh3	Derived available soil water capacity (volumetric fraction) with FC = pF 2.5
	WWP	Derived available soil water capacity (volumetric fraction) until wilting point
	AWCtS	Saturated water content (volumetric fraction) teta-S

Terrain feature	elevation	Elevation (in m)

179

180　At the global scale, the input features are collected from the same sources as the local scale except for PFT and

181　elevation. We extract PFT from MODIS 1km land cover type product (MCD12Q1) in 2001 (downloaded via

182　Google Earth Engine) and apply the elevation product derived from the SRTM data at 0.0083 degrees

183　(downloaded from https://www.worldclim.org/data/worldclim21.html). All global input features are resampled

184　to the spatial resolution of 1km based on the linear interpolation approach.

185　All input features are normalized and then standardized by subtracting the mean and dividing by the standard

186　deviation. The categorical variables were processed based on the one-hot encoding approach.

187　2.4　Simultaneous parameter inversion and extrapolation (SPIE)

188　The SPIE approach is to inverse and extrapolate parameters based on a hybrid model coupling a traditional

189　process model and a neural network[37]. Here, we couple the LUE model with a multilayer perceptron neural

190　network (3 hidden layers and 64 neurons per layer). All LUE model parameters and WAI parameters are

191　predicted using the neural network based on standardized input features. The predicted parameters are then used

192　to parameterize the LUE model and WAI to estimate GPP and ET with the temporal forcing data from EC sites

193　(as explained 2.2). We optimized and constrained the neural network by the cost function including GPP errors

194　(sum of the squared difference between GPP_{obs} and GPP_{sim} divided by the uncertainty of NEE), ET errors (sum

195　of the squared difference between ET_{obs} and ET_{sim} divided by the uncertainty of LE) and some constraints on

196　sensitivity functions (see equations S1-S5). The outputs of the whole framework include the predicted

197　parameters (only spatially changed) and the estimated temporal GPP and ET (see the flowchart in Bao et al.,

198　2023). Since the neural network is trained against the observations and learns the relationship between the input

199　features and model parameters, it is applied to analyze the spatial variability and extrapolate the parameters.

200　To avoid the effect of different training datasets on the learned relationship, we trained the neural network ten

201　times based on different groups of datasets. Each training dataset covered all PFTs and climate types of the sites

202　comprehensively to reduce extrapolation bias. GPP_{sim} and ET_{sim} are validated according to the ten-fold cross-

203　validation strategy. The following results and analyses are all based on the cross-validated parameters and GPP.

204　2.5　　Partial dependence plot (PDP)

205　The partial dependence plot (PDP) is a typical approach to analyze the responses of predictions to the input

206　features of interest for interpreting a machine learning model[38]. We compute the partial dependence of the

207　predicted model parameters on each input feature. First, we generate a sequence of 100 numbers with the same

208　interval within the range of an input feature across sites while fixing other features. The combinations of the

209　generated feature and the other features are inputted into the trained neural network to predict parameters of test

210　sites (refers to datasets excluded in the training process). The trend of the predicted parameters, which is shown

211　in PDP, indicates the response of the parameter to the change in the generated feature, marginalizing all other

212　input features. For categorical features (PFT and climate types), the partial dependence is calculated based on

213　two values of the target feature (0 and 1) combined with other features.

214　2.6　　Shapley additive explanation (SHAP) dependence plot

215　The Shapley additive explanation (SHAP) dependence plot is an alternative to PDP for the global interpretation

216　of machine learning models. The Shapley value of each feature is calculated based on the deviation of the

217　predicted model parameter at a certain input from the average prediction[39]. Shapley values represent the

218　contribution of a feature to the predicted parameter. We analyze the response of parameters by the average

219　Shapley value across sites of each feature, i.e., the SHAP dependence plot. Since the Shapley value shows the

220　variance of predictions while partial dependence shows the average effects, we subtract the mean from the partial

221　dependence and divide it by the number of input features to make the PDP and SHAP comparable.

222　2.7　　Uncertainty assessment

223　We assessed uncertainties in predicted GPP and parameters with respect to training datasets and neural network

224　structures.

225　The sites were divided into ten groups randomly for cross-validation. We trained SPIE using every nine of these

226　groups as the training dataset (10% of the training datasets were set as the test dataset to tune the neural network)

227　and validated the remaining group as the test dataset until all groups were validated independently. The

228　uncertainties in parameters and GPP arising from different training datasets were quantified using the standard

229 deviation of parameter scalars and the Nash-Sutcliffe model efficiency (NSE) of estimated GPP across these ten

230 site groups.

231 We assessed the epistemic uncertainty of the neural network (due to structures and parameters) by applying

232 drop-out training as a Bayesian approximation[40]. The drop-out training was repeated ten times to calculate the

233 standard deviation of NSE and parameter scalars as the neural network uncertainty.

3. Results

235 3.1   Performance of SPIE

236 The simulation accuracy of GPP showed that SPIE performed well at different time scales (Figure 2). NSE and

237 determination coefficient (R^2) of the mean GPP per day of year, week and month across sites reached 0.78, 0.79

238 and 0.80 respectively (Figure 2a-c). At the annual scale, the NSE and R^2 of GPP_{sim} were not as good as shorter

239 time scales, but the normalized root mean squared error was lower (NRMSE=0.31). At the site level, SPIE can

240 perform well (NSE>0) at 78%, 74%, 58% and 21% of the sites at daily, weekly, monthly and annual scales,

241 respectively. As another output of the LUE model, the simulation accuracy of ET was also good

242 (NSE=0.55,0.57,0.59 and 0.35). Although the GPP_{sim} based on SPIE (in cross-validation) underperformed site

243 calibrations (trained on all sites), SPIE overperformed using optimized parameters per PFT (OPT-PFT, shown

244 in Figure S1), which is widely applied in most photosynthesis models. It illustrates that the seasonal variability

245 of GPP using the SPIE-predicted parameters can be well captured with a low mean annual error.
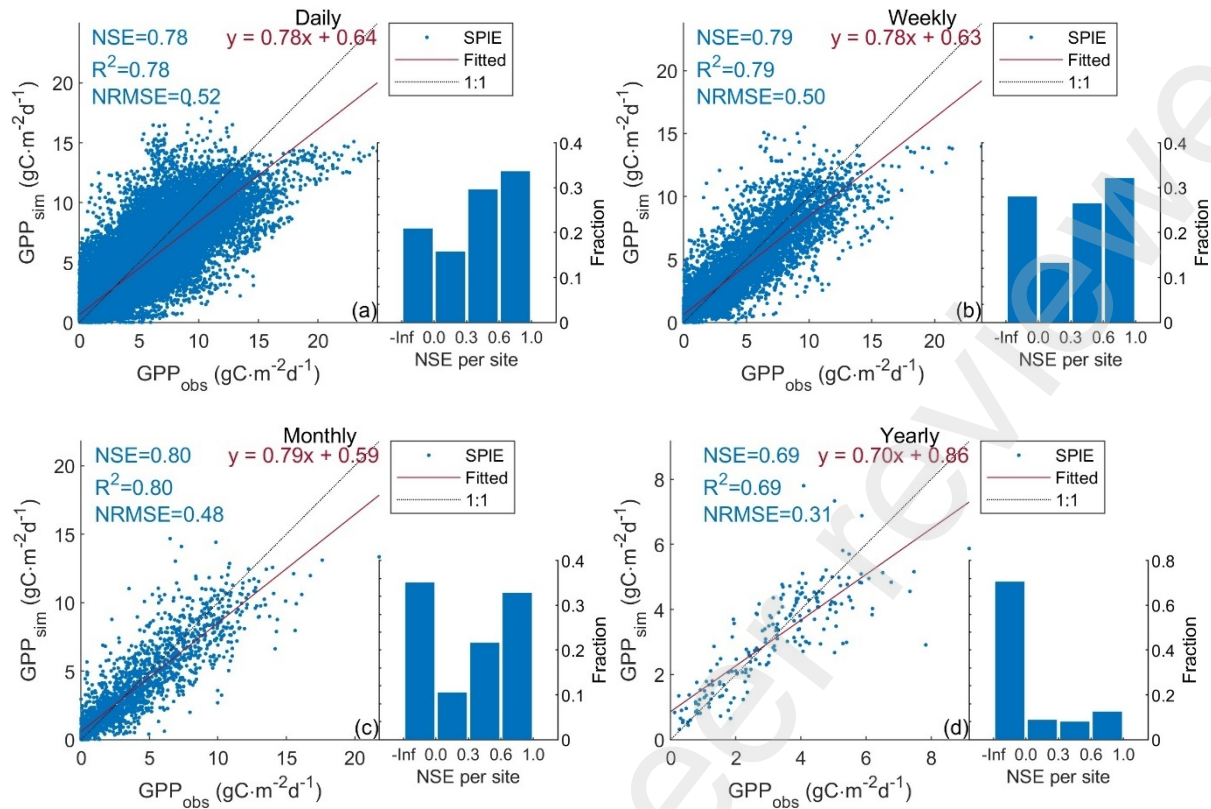
**Figure 2. Comparison between mean seasonal cycle GPP$_{obs}$ and GPP$_{sim}$ based on SPIE-predicted parameters (in blue).** Each scatter represents the mean GPP per Julian day, week, month or per year at a site, respectively. The histogram is the distribution of the site-level NSE at daily, weekly, monthly and annual scales, respectively.

3.2   Response of water sensitivity parameters to model inputs

The spatial variability of W_I and k_W were both dominated by vegetation features, soil properties and climatic characteristics. According to two-sample Kolmogorov-Smirnov tests, MF and DBF had significantly smaller W_I and k_W than other types (Figure 3(1) and Figure 4(1)), indicating generally fewer water limitations and faster responses to changes in water availability. WET also had statistically smaller W_I. The differences between other PFTs were not statistically significant, while the mean and median of W_I in shrublands (OSH and CSH) and GRA sites were larger, representing greater water constraints in most of the sites. The partial dependence plots showed that the variability of W_I and k_W was primarily contributed by vegetation seasonality, forest age, bioclimatic conditions, soil properties and aridity seasonality. The higher VIF2 (=standard deviation of EVI) related to greater water limitation and faster-responding speed to soil water availability (i.e., larger W_I and k_W, Figure 3(2) and Figure 4(2)), whereas higher AI2 (=standard deviation of monthly aridity index) resulted in

263   lower limitation and responding speed (Figure 3(10) and Figure 4(8)). Older forests (50-300 years) exhibited

264   lower W_I and k_W than younger forests in the range of 0-50 years. Besides, W_I and k_W were strongly correlated to

265   the precipitation in the coldest quarter and the mean temperature of the driest quarter (BIO19 and BIO9). The

266   temperature in the warmest month and quarter (BIO5 and BIO10) and mean annual temperature (BIO1) all had

267   positive effects on the parameters, representing the temperature can increase the average water limitation on

268   GPP and response speed to variations in soil water availability. The influence of various soil property variables

269   on W_I and k_W were different, while the variables related to water holding capacity contributed the most to the

270   variability for W_I and k_W, e.g., CRFVOL and BDTICM. In general, vegetation features, including PFT,

271   vegetation index features and forest age, together with climate features as well as soil properties, were driving

272   the spatial variability of W_I and k_W.

273
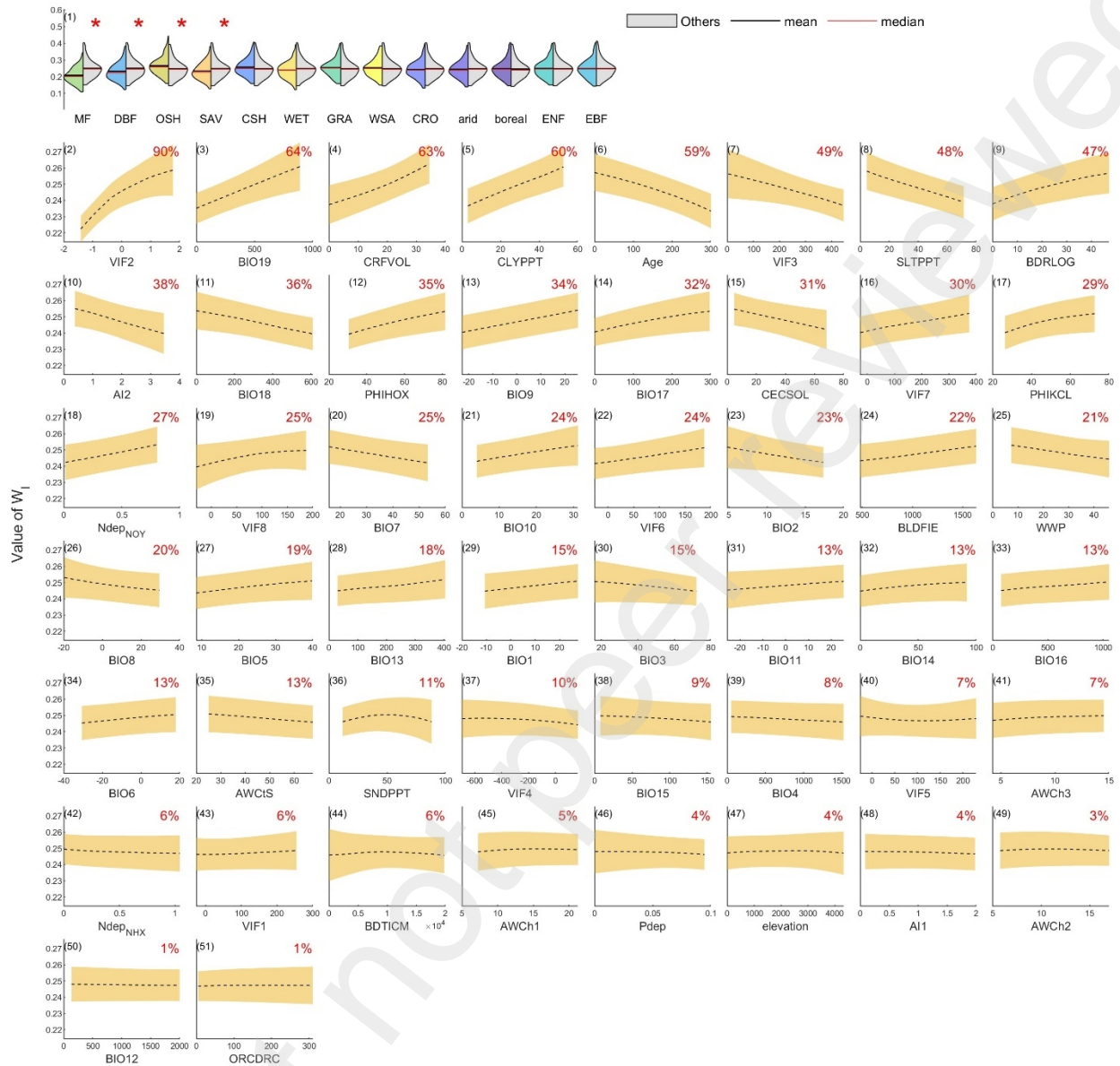
Figure 3. Partial dependence plots of W_I to input features in cross-validation. Categorical features (the first row, (1)) are arranged by the differences between means of predicted W_I, with the red asterisk indicating statistically significant differences ($p<0.05$) between predicted W_I of a specific type and those of other types (grey-color). The width of the half violin plots indicates the probability density function. Non-categorical features are sorted by the relative variance (shown in the upper-right corner of (2)- (51)). The brown shadow in (2)- (51) represents the standard deviation of the predicted W_I across training groups.

280

Figure 4. Partial dependence plots of k_W to input features in cross-validation.

The parameter indicating the lagged response of GPP to soil moisture change, α_W, was mainly controlled by vegetation features including PFTs and EVI features, bioclimatic variables and soil properties (Figure 5). The α_W of OSH sites was significantly higher than others, representing OSH were more likely to have lagged responses, in opposite to DBF sites. The seasonality of vegetation dominates the variability of α_W, which was the same as W_I and k_W. Besides, the responses of α_W to the mean EVI in the wettest quarter (VIF5) and the maximum EVI in the warmest month (VIF3) showed that dense vegetation with higher maximum and mean EVI can respond to soil moisture promptly, while sparse vegetation was more prone to exhibit a lag effect. The lag effect was also related to the thermal conditions (e.g., BIO5, BIO10, BIO2 and BIO7). It showed that hot

290   temperatures and larger diurnal and annual temperatures can result in lagged responses of GPP to soil moisture.

291   Furthermore, α_W was affected by the soil properties related to water and nutrient holding capacity and soil PH,

292   like CECSOL, CLYPPT, SLTPPT, and PHIKCL. The vegetation growing in the environment with higher aridity

293   (lower AI1) and lower aridity seasonality (lower AI2) had higher α_W, representing more likely to have lagged

294   responses. Alpine vegetation also had higher α_W. In general, the dominant variables of α_W were similar to part

295   of the dominant variables of W_I and k_W, like PFTs and soil water holding capacity, however, α_W was more

296   influenced by the maximum and mean EVI and thermal conditions.
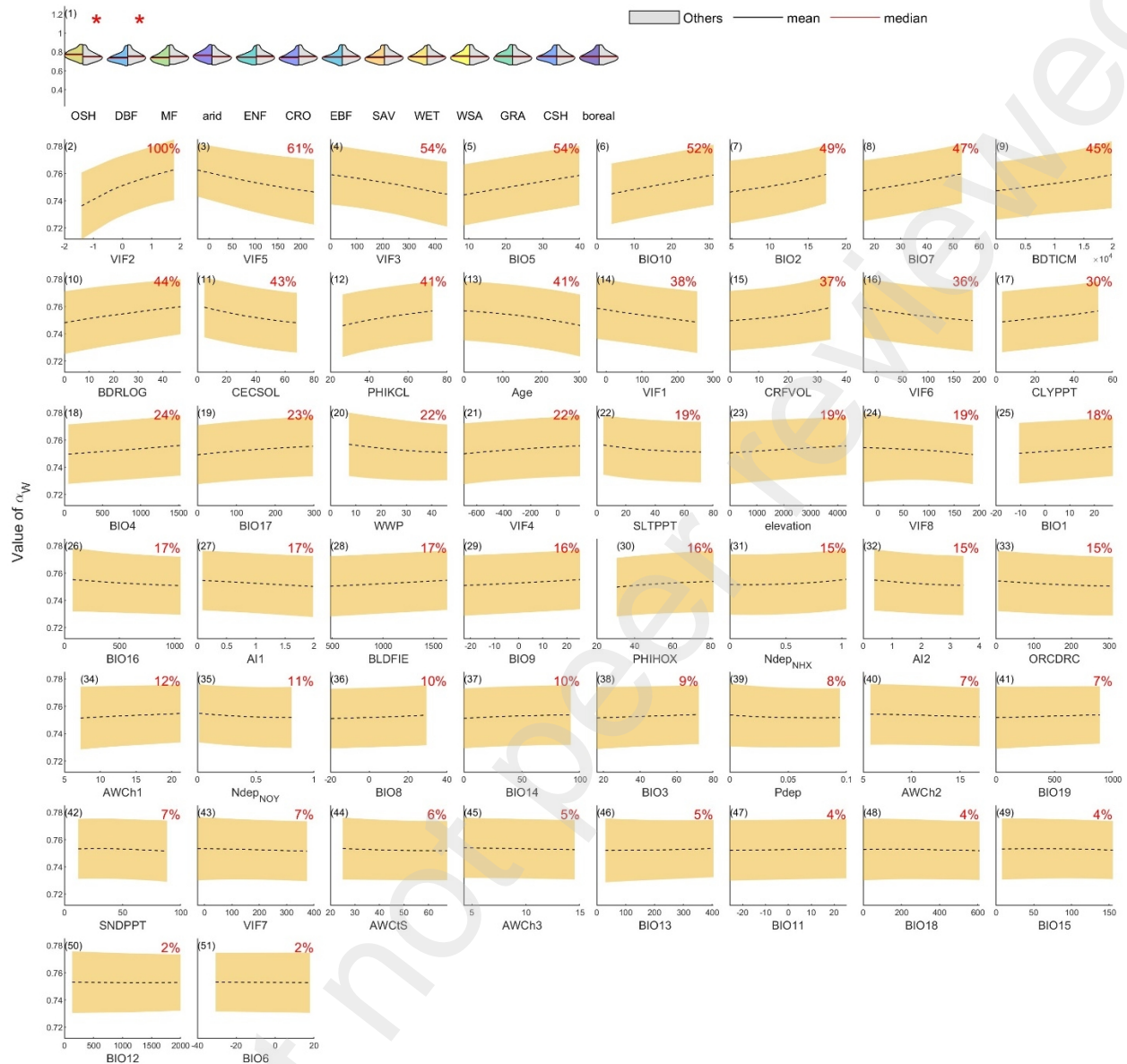
Figure 5. Partial dependence plots of α_W to input features in cross-validation

The SHAP dependence plots presented different magnitudes but similar trend directions to the PDP. Although the magnitudes and slopes were slightly different, the changing trends of parameters to various features were the same after converting the units of partial dependences to Shapley values (Figure S2-7). Thus, the derived response trends were robust between different approaches and training datasets.

To summarize, the parameters controlling soil water sensitivity, W_I, k_W and α_W, strongly responded to the vegetation seasonality and soil properties relating to the water holding capacity. Shrubs generally face greater

305 water limitation compared to other plant types, whereas deciduous broadleaf and mixed forests exhibit faster

306 responses to changes in soil water availability than other plant types.

307 3.3 Uncertainties in GPP and parameters

308 At the site level, low uncertainties in GPP and predicted parameters associated with training datasets and neural

309 network structures were observed (Figure 6). The mean seasonal cycle GPP showed robustness at daily, weekly

310 and monthly scales (standard deviation of NSE<0.01 and 0.08, respectively), while at the annual scale, the

311 uncertainty was over twice as high. The uncertainties in predicted W_I, k_W and α_W using different training datasets

312 and neural network structures were similar. Both results showed that the uncertainty of predicted k_W was higher

313 than the other two parameters.

314

315
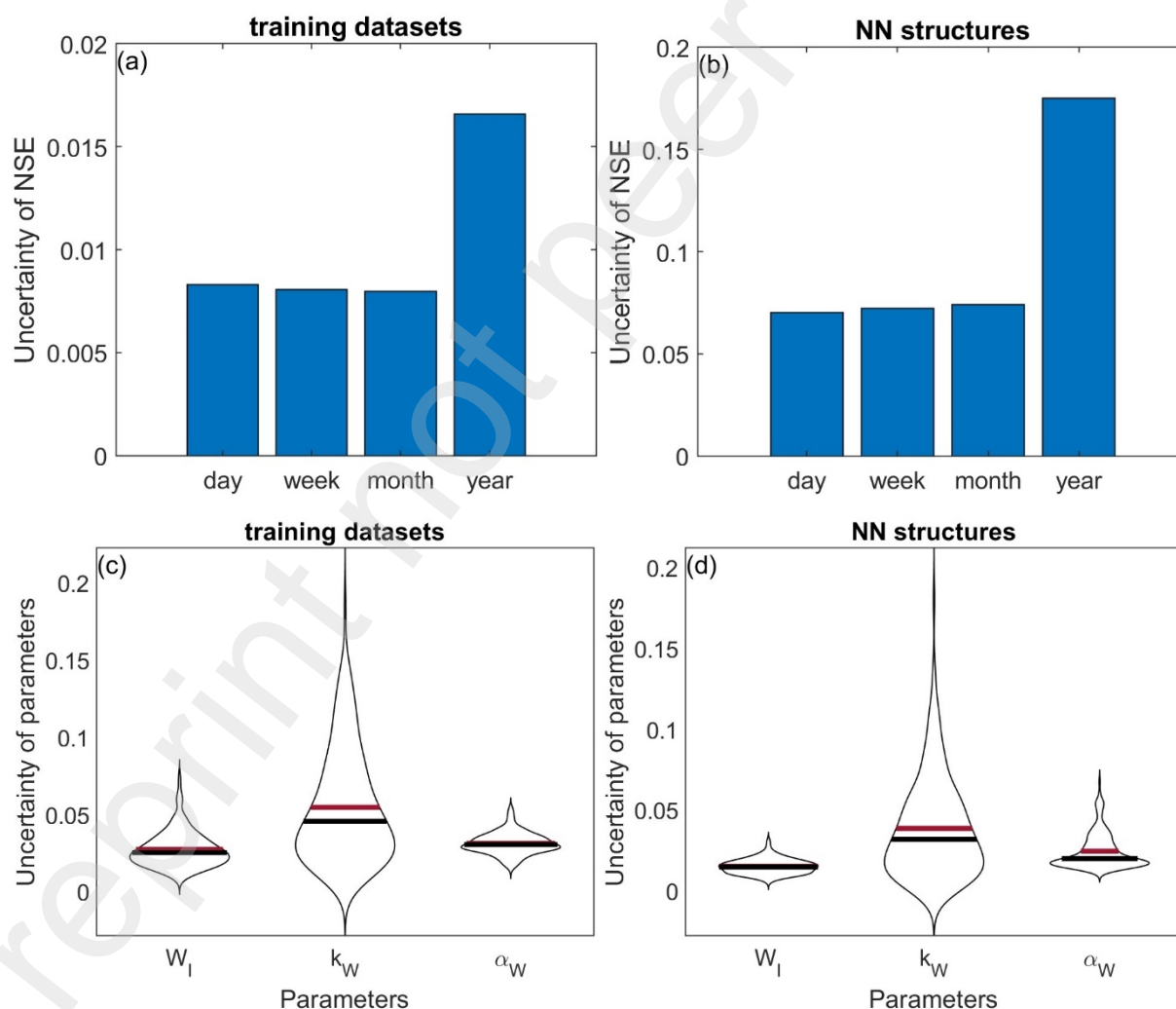
Figure 6. Uncertainty in Nash-Sutcliffe efficiency (NSE) of mean seasonal cycle GPP and predicted parameters due to different training datasets and neural network structures.

At the global scale, the uncertainty related to training datasets and neural network structures both showed spatial heterogeneity. The uncertainty of W_I and k_W resulting from different training datasets was higher in the tropics and polar regions due to less data (Figure S8a-b). For the same reason, α_W exhibited higher uncertainties in the west of Asia (Figure S8c). The median uncertainty of W_I and k_W reached 13% and 28%, respectively, much higher than α_W (=3%). Compared to the uncertainty from training datasets, lower W_I, k_W and α_W uncertainties from neural network structures were observed (median=10%, 21% and 2%, respectively). The W_I and α_W uncertainty was relatively homogeneous spatially, whereas k_W displayed lower uncertainties in arid regions and higher uncertainties in other places (Figure S9). Our results reflected that parameter uncertainties were affected by the distribution density of training datasets.
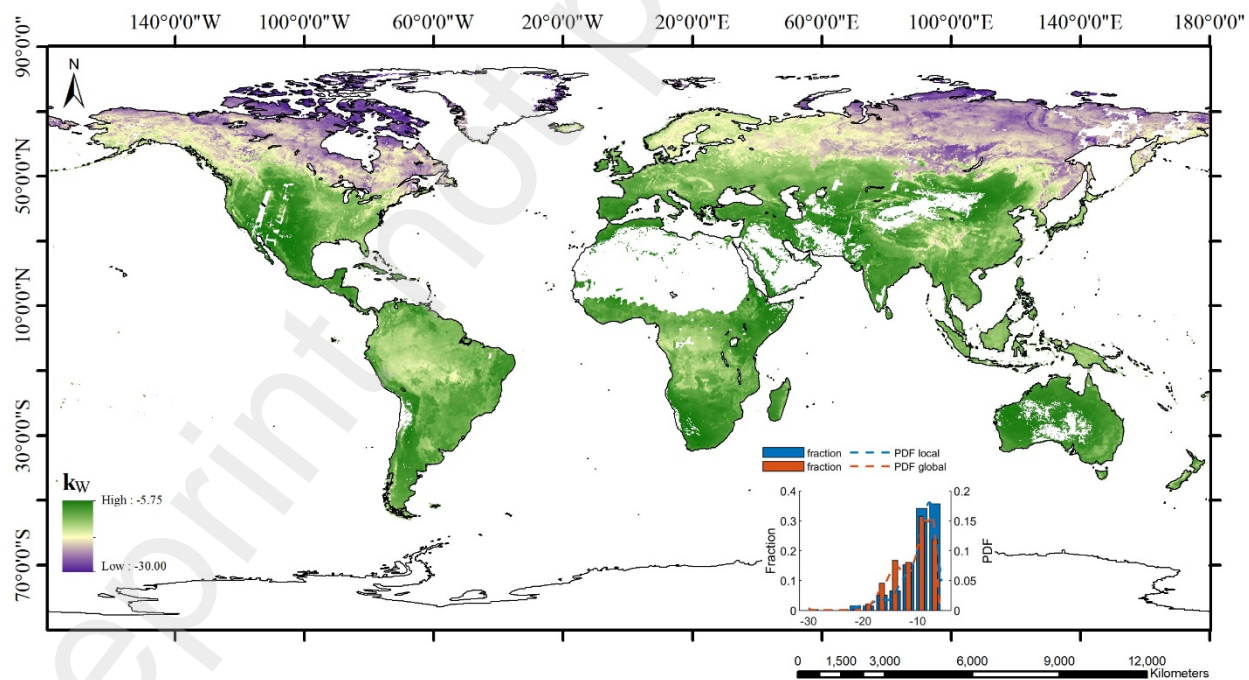
3.4   Global distribution maps

The global distribution of W_I and k_W shows higher water constraints and quicker responses to soil water in subtropical and temperate dry regions while lower in the wet tropics and high northern latitudes. The high W_I was observed primarily in the south of North America, areas around the Mediterranean Sea, West Asia and North Africa (Figure 7a). In these places, k_W was also high (Figure 7b), indicating more significant water limitation and slower responding speed. W_I and k_W were strongly correlated in 55% of the areas (r>0.7). Besides, we found high α_W values (median=0.83) across all arid climates (according to the Koeppen-Geiger climate classification, Figure 7c). It represented that most vegetation growing under arid climates exhibited lagged responses to soil moisture. Furthermore, the global k_W showed a slightly different density distribution pattern from the local scale (see the histogram in Figure 7b). In general, the global maps illustrated that GPP in arid regions experiences greater water limitations and exhibits both gradual and delayed responses to water availability.
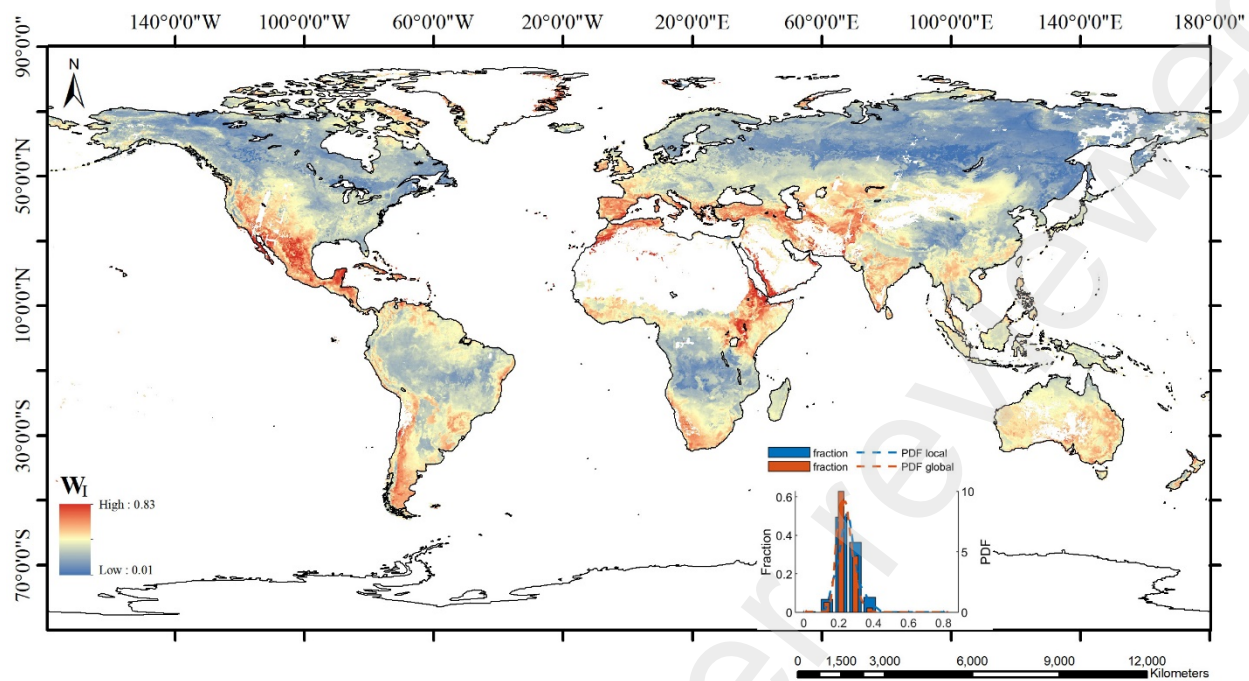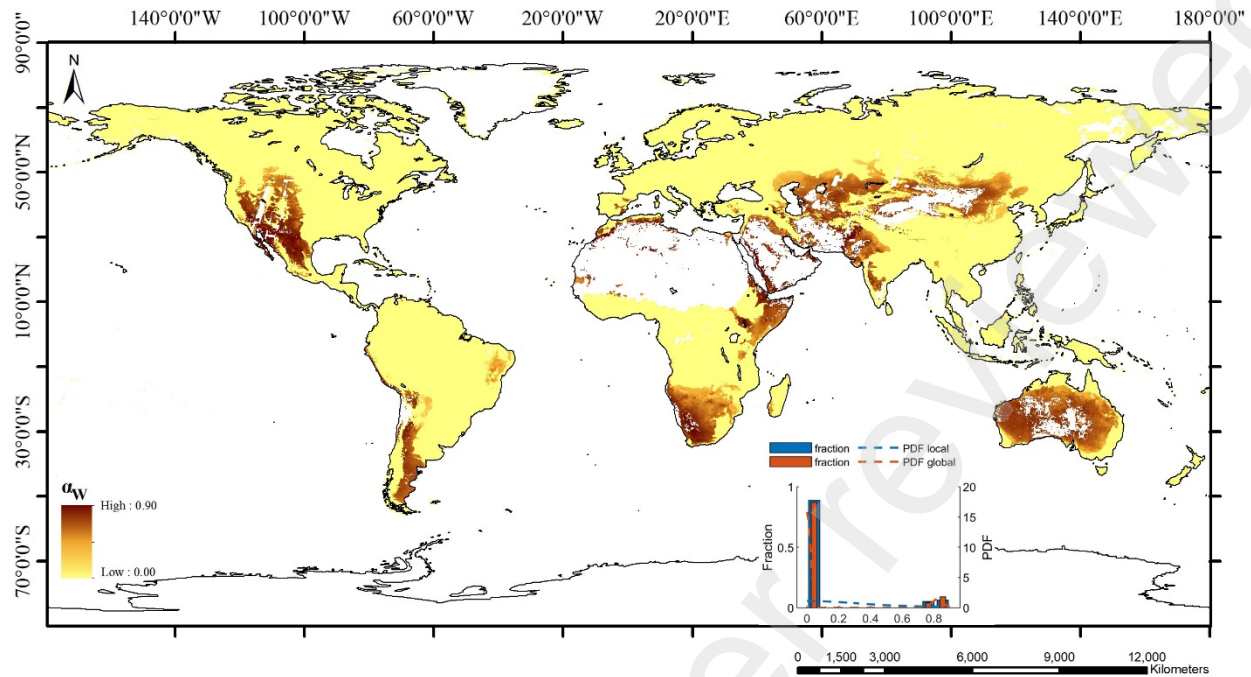
338

339

(a)

340

341

(b)

342

343 (c)

344 **Figure 7. Global distribution maps of (a)W_I, (b)k_W and (c)α_W in 0.0083° (**smoothed using a 25*25 moving
345 median window)**.** The histogram shows the possibility distribution function (PDF, dotted lines) and fraction
346 (bars) of the predicted parameters at sites (in blue) and at the global scale (in red).

4. Discussion

348 4.1 Drivers for GPP sensitivities to soil water availability

349 Vegetation water sensitivities differ between plant types. Our results reveal that forests, especially MF and DBF,

350 face statistically fewer water limitations and respond faster to water availability changes, while grass and shrubs

351 tend to be more insensitive to water availability changes, similar to the findings of another study[41]. This can

352 be related to vegetation physiological features, climate and soil properties of the growing environment.

353 Vegetation index features, especially VIF2 representing vegetation seasonality strength, were found to be the

354 most important variables to predict W_I, k_W, and α_W, in other words, to control the water sensitivity of GPP. On

355 the one hand, the importance can be explained by the interaction (i.e., a vegetation index influences carbon

356 assimilation rate and is affected by carbon allocation) and strong correlation between GPP and a vegetation index

357 (here refers to EVI). On the other hand, the vegetation variability, which is related to species and climates,

358   influences the response of GPP under water stress[42]. Our results indicate that vegetation with lower seasonal

359   variability experiences fewer water constraints generally and GPP saturates faster than vegetation with higher

360   seasonal variability.

361   Stand age is another important feature affecting the inflection point and the slope of soil water response function,

362   i.e., W_I and k_W. Older trees generally experience lower water limitations and respond faster to soil moisture

363   changes relative to younger trees. Our findings agree with on-site studies of trees older than 25 years[43],

364   showing higher average soil moisture content for older trees. The wetness of environments for older trees

365   (e.g., >50 years) like rainforests could also contribute.

366   Soil properties were known to have important effects on vegetation responses to water stress[44]. Soil water

367   holding capacity, indicating the maximum water content the soil can hold under gravity, is related to soil

368   properties such as soil depth and soil texture. However, the water availability for plants might not be positively

369   correlated with soil water holding capacity due to variations in soil water matric potential[45]. Although the W_I,

370   k_W, and α_W were all controlled by properties relating to the soil water holding capacity, the relationships can be

371   opposite. For example, soils with fewer coarse fragments, higher clay content and deeper depth tend to have

372   higher water-holding capacity. However, the relationship between W_I and coarse fragments, between W_I and

373   soil clay content and between k_W and soil depth (Figure 3 (4)- (5) and Figure 4 (2)) were all positive. The findings

374   demonstrated that the spatial relationship between vegetation water sensitivity and soil properties were strongly

375   affected by other factors dominating soil water matrix potential, such as vegetation type, rainfall and soil

376   temperature[44, 46].

377   Bioclimatic variables are the last but not the least key factors for the soil water response function. Our results

378   showed the rising annual and seasonal temperature (e.g., BIO1, BIO5, and BIO9-10), especially in the warmest

379   and driest seasons, can exacerbate water limitations and reduce the GPP saturation speed. Additionally, the rising

380   temperature can intensity the lag in GPP responses due to green tissue redevelopment following drought periods.

381   Greater seasonality and variability in annual temperature (e.g., BIO2-4 and BIO7) correlate with reduced water

382   constraints but are associated with more pronounced lagged responses. Furthermore, the spatial correlation

383   between rainfall and GPP's responses to water availability exhibits complexity. An increase in rainfall does not

384   uniformly reduce water sensitivity across large spatial extents, likely influenced by diverse soil properties[44]

385   and the mitigation of evapotranspiration. This contrasts with the more direct and immediate temporal correlation

386   between rainfall and vegetation water stress [47]. Hence, the patterns of spatial variation in water sensitivity of

387   GPP cannot be straightforwardly translated to temporal analyses. Our study confirms temperature as a main

388   driver of soil water sensitivities across the sites.

389   4.2   Spatial patterns of GPP sensitivity to soil water availability

390   The global distribution pattern of W_I and k_W generally follows the climate aridity[48, 49]. It is also similar to the

391   pattern of precipitation sensitivity to leaf area index changes[figure 2a in 50], reflecting the spatial variability of

392   vegetation sensitivities to water supply. However, the pattern is different from the root-zone water storage

393   estimated by the maximum cumulative water deficit during dry seasons[24], particularly in the subtropical dry

394   regions (e.g., southern Spain, India and South Asia). In most of the arid areas, the response of GPP to water

395   availability changes has a temporal lag (brown area in Figure 7c). This lag effect is associated with the

396   vegetation's strategy to mitigate water stress resulting from insufficient rainfall or alterations in its

397   seasonality[51]. The strategy is a result of a plant's system to absorb and recover from disturbance or stress[52,

398   53]. The phenomenon in local scales has been reported in other studies[25, 53, 54]. Our results reveal the spatial

399   relationship between the response of GPP to soil water availability and water supply.

400   4.3   Challenges in parameter interpretation

401   The uncertainties in parameters due to training datasets and neural network structures cannot be neglected in

402   tropics and humid areas, respectively. The predicted GPP contains the uncertainty introduced by the parameters.

403   Although the relative importance of the input features (i.e., the magnitude of the partial dependence and SHAP

404   dependence) differ across approaches and datasets, our results show stable trend directions of dependence plots.

405   Nevertheless, several challenges require further investigation in future studies.

406   The performance of simulated GPP by SPIE is good across sites (NSE=0.78), while it is low (NSE≤0) at 21%

407   of the sites, particularly for evergreen broadleaf forest, tropical and polar sites where the uncertainty is relatively

408   high. This may hamper the analysis of parameter variability in these sites and increase the error and uncertainty

409   in wet tropics and the Arctic. In general, SPIE works well spatially while needs further improvement to capture

410   the temporal variability of GPP for evergreen broadleaf forests, tropics and polar regions.

411   In addition to instantaneous responses to environmental changes, plants undergo physiological and structural

412   adaptions over weekly to monthly time scales to optimize their growth potential during their lifetime, i.e.,

413   acclimation[55, 56]. Mengoli et al.[57] demonstrated the importance of incorporating temperature acclimation

414   by dynamically adjusting parameters representing the maximum carboxylation and electron transport rates,

415   leading to improvement in model performance. This highlights the necessity of considering the acclimation of

416   model parameters, i.e., the temporal variability of parameters, in future studies.

417   **5. Conclusion**

418   Our study highlights that the response of GPP to soil water availability is influenced by several factors, including

419   plant types, vegetation seasonality, soil properties and bioclimatic conditions. Especially, older forests, and

420   vegetation with lower seasonal variability generally exhibits fewer water limitations and GPP reach saturations

421   faster, contrasting with more gradual responses observed in grass and shrubs. Furthermore, soil properties,

422   particularly those related to soil water holding capacity, play a significant role in shaping GPP responses,

423   nevertheless the relationship between them is complex. We also found that higher annual and seasonal

424   temperatures intensity average water limitations and reduce the GPP saturation rate. Additionally, arid plant GPP

425   responses to water availability show lagged effect. The spatial distribution pattern of GPP response to water

426   availability generally aligns with the climate aridity. Our study identifies consistent patterns across the space,

427   regardless of training datasets and neural network structures, while uncertainties exist at local scales. These

428   findings underscore the importance of considering plant types, vegetation features, soil properties and

429   bioclimatic conditions when analyzing the spatial variability of responses of carbon assimilation to water stress

430   under global climate changes.

431   **References**

432   1.   Jung, M., et al., *Compensatory water effects link yearly global land CO2 sink changes to temperature.*
433   Nature, 2017. **541**(7638): p. 516-520.

434 2.   Humphrey, V., et al., *Soil moisture–atmosphere feedback dominates land carbon uptake variability.*
435   Nature, 2021. **592**(7852): p. 65-69.
436 3.   Gampe, D., et al., *Increasing impact of warm droughts on northern ecosystem productivity over recent*
437   *decades.* Nature Climate Change, 2021. **11**(9): p. 772-779.
438 4.   Li, W., et al., *Widespread and complex drought effects on vegetation physiology inferred from space.*
439   Nature Communications, 2023. **14**(1): p. 4640.
440 5.   Stocker, B.D., et al., *Quantifying soil moisture impacts on light use efficiency across biomes.* New
441   Phytologist, 2018. **218**(4): p. 1430-1449.
442 6.   Greve, P., et al., *Global assessment of trends in wetting and drying over land.* Nature Geoscience, 2014.
443   **7**(10): p. 716-721.
444 7.   Monteith, J.L., *Solar radiation and productivity in tropical ecosystems.* Journal of applied ecology, 1972.
445   **9**(3): p. 747-766.
446 8.   Running, S.W., et al., *A continuous satellite-derived measure of global terrestrial primary production.*
447   Bioscience, 2004. **54**(6): p. 547-560.
448 9.   Yuan, W., et al., *Global comparison of light use efficiency models for simulating terrestrial vegetation*
449   *gross primary production based on the LaThuile database.* Agricultural and Forest Meteorology, 2014.
450   **192**: p. 108-120.
451 10. Stocker, B.D., et al., *P-model v1. 0: an optimality-based light use efficiency model for simulating ecosystem*
452   *gross primary production.* Geoscientific Model Development, 2020. **13**(3): p. 1545-1581.
453 11. Farquhar, G.D., S.v. von Caemmerer, and J.A. Berry, *A biochemical model of photosynthetic CO 2*
454   *assimilation in leaves of C 3 species.* planta, 1980. **149**: p. 78-90.
455 12. Lawrence, D.M., et al., *The Community Land Model Version 5: Description of New Features,*
456   *Benchmarking, and Impact of Forcing Uncertainty.* Journal of Advances in Modeling Earth Systems, 2019.
457   **11**(12): p. 4245-4287.
458 13. Sitch, S., et al., *Evaluation of the terrestrial carbon cycle, future plant geography and climate‐carbon cycle*
459   *feedbacks using five Dynamic Global Vegetation Models (DGVMs).* Global change biology, 2008. **14**(9): p.
460   2015-2039.
461 14. Eyring, V., et al., *Overview of the Coupled Model Intercomparison Project Phase 6 (CMIP6) experimental*
462   *design and organization.* Geoscientific Model Development, 2016. **9**(5): p. 1937-1958.
463 15. Groenendijk, M., et al., *Assessing parameter variability in a photosynthesis model within and between*
464   *plant functional types using global Fluxnet eddy covariance data.* Agricultural and forest meteorology,
465   2011. **151**(1): p. 22-38.
466 16. Carvalhais, N., et al., *Deciphering the components of regional net ecosystem fluxes following a bottom-up*
467   *approach for the Iberian Peninsula.* Biogeosciences, 2010. **7**(11): p. 3707-3729.
468 17. Mäkelä, A., et al., *Developing an empirical model of stand GPP with the LUE approach: analysis of eddy*
469   *covariance data at five contrasting conifer sites in Europe.* Global change biology, 2008. **14**(1): p. 92-108.
470 18. Yuan, W., et al., *Increased atmospheric vapor pressure deficit reduces global vegetation growth.* Science
471   advances, 2019. **5**(8): p. eaax1396.
472 19. Zhou, Y., et al., *Global parameterization and validation of a two‐leaf light use efficiency model for*
473   *predicting gross primary production across FLUXNET sites.* Journal of Geophysical Research:
474   Biogeosciences, 2016. **121**(4): p. 1045-1072.
475 20. Wang, H., et al., *Towards a universal model for carbon dioxide uptake by plants.* Nature plants, 2017. **3**(9):
476   p. 734-741.
477 21. Madani, N., et al., *Improving ecosystem productivity modeling through spatially explicit estimation of*
478   *optimal light use efficiency.* Journal of Geophysical Research: Biogeosciences, 2014. **119**(9): p. 1755-1769.
479 22. Wang, H., et al., *Deriving maximal light use efficiency from coordinated flux measurements and satellite*
480   *data for regional gross primary production modeling.* Remote Sensing of Environment, 2010. **114**(10): p.
481   2248-2258.
482 23. Croft, H., et al., *Leaf chlorophyll content as a proxy for leaf photosynthetic capacity.* Global change
483   biology, 2017. **23**(9): p. 3513-3524.
484 24. Stocker, B.D., et al., *Global patterns of water storage in the rooting zones of vegetation.* Nature
485   Geoscience, 2023. **16**(3): p. 250-256.
486 25. Horn, J. and K. Schulz, *Spatial extrapolation of light use efficiency model parameters to predict gross*
487   *primary production.* Journal of Advances in Modeling Earth Systems, 2011. **3**(4).

488   26.   Peaucelle, M., et al., *Covariations between plant functional traits emerge from constraining*
489   *parameterization of a terrestrial biosphere model.* Global Ecology and Biogeography, 2019. **28**(9): p.
490   1351-1365.

491   27.   Bao, S., et al., *Toward Robust Parameterizations in Ecosystem-Level Photosynthesis Models.* Journal of
492   Advances in Modeling Earth Systems, 2023. **15**(8): p. e2022MS003464.

493   28.   Bao, S., et al., *Environment-sensitivity functions for gross primary productivity in light use efficiency*
494   *models.* Agricultural and Forest Meteorology, 2022. **312**: p. 108708.

495   29.   Tramontana, G., et al., *Predicting carbon dioxide and energy fluxes across global FLUXNET sites with*
496   *regression algorithms.* Biogeosciences, 2016. **13**(14): p. 4291-4313.

497   30.   Trautmann, T., et al., *The importance of vegetation in understanding terrestrial water storage variations.*
498   Hydrol. Earth Syst. Sci., 2022. **26**(4): p. 1089-1109.

499   31.   Walther, S., et al., *A view from space on global flux towers by MODIS and Landsat: the FluxnetEO dataset*
500   *(Landsat)*, in *Biogeosciences*. 2022. p. 2805-2840.

501   32.   Fick, S.E. and R.J. Hijmans, *WorldClim 2: new 1 km spatial resolution climate surfaces for global land*
502   *areas.* International journal of climatology, 2017. **37**(12): p. 4302-4315.

503   33.   Zomer, R.J., J. Xu, and A. Trabucco, *Version 3 of the global aridity index and potential evapotranspiration*
504   *database.* Scientific Data, 2022. **9**(1): p. 409.

505   34.   Besnard, S., et al., *Mapping global forest age from forest inventories, biomass and climate data.* Earth
506   System Science Data, 2021. **13**(10): p. 4881-4896.

507   35.   Rodhe, H., F. Dentener, and M. Schulz, *The global distribution of acidifying wet deposition.* Environmental
508   Science & Technology, 2002. **36**(20): p. 4382-4388.

509   36.   Poggio, L., et al., *SoilGrids 2.0: producing soil information for the globe with quantified spatial*
510   *uncertainty.* Soil, 2021. **7**(1): p. 217-240.

511   37.   Bao, S., et al., *Towards Robust Parameterizations in Ecosystem-level Photosynthesis Models.* Journal of
512   Advances in Modeling Earth Systems, 2023. **15**(8): p. e2022MS003464.

513   38.   Friedman, J.H., *Greedy function approximation: a gradient boosting machine.* Annals of statistics, 2001: p.
514   1189-1232.

515   39.   Lundberg, S.M. and S.-I. Lee, *A unified approach to interpreting model predictions*, in *Proceedings of the*
516   *31st International Conference on Neural Information Processing Systems*. 2017, Curran Associates Inc.:
517   Long Beach, California, USA. p. 4768–4777.

518   40.   Gal, Y. and Z. Ghahramani. *Dropout as a bayesian approximation: Representing model uncertainty in deep*
519   *learning*. in *international conference on machine learning*. 2016. PMLR.

520   41.   Whitecross, M., E. Witkowski, and S. Archibald, *Savanna tree-grass interactions: A phenological*
521   *investigation of green-up in relation to water availability over three seasons.* South African Journal of
522   Botany, 2017. **108**: p. 29-40.

523   42.   Yu, T., et al., *Interannual and seasonal relationships between photosynthesis and summer soil moisture in*
524   *the Ili River basin, Xinjiang, 2000–2018.* Science of The Total Environment, 2023. **856**: p. 159191.

525   43.   Jia, X., et al., *Soil moisture decline due to afforestation across the Loess Plateau, China.* Journal of
526   Hydrology, 2017. **546**: p. 113-122.

527   44.   Fernandez-Illescas, C.P., et al., *The ecohydrological role of soil texture in a water-limited ecosystem.* Water
528   Resources Research, 2001. **37**(12): p. 2863-2872.

529   45.   Whalley, W.R., E.S. Ober, and M. Jenkins, *Measurement of the matric potential of soil water in the*
530   *rhizosphere.* Journal of Experimental Botany, 2013. **64**(13): p. 3951-3963.

531   46.   Chow, T.L., et al., *Effects of coarse fragment content on soil physical properties, soil erosion and potato*
532   *production.* Canadian Journal of Soil Science, 2007. **87**(5): p. 565-577.

533   47.   Park Williams, A., et al., *Temperature as a potent driver of regional forest drought stress and tree*
534   *mortality.* Nature Climate Change, 2013. **3**(3): p. 292-297.

535   48.   Ullah, S., et al., *Spatiotemporal changes in global aridity in terms of multiple aridity indices: An*
536   *assessment based on the CRU data.* Atmospheric Research, 2022. **268**: p. 105998.

537   49.   Asadi Zarch, M.A., B. Sivakumar, and A. Sharma, *Assessment of global aridity change.* Journal of
538   Hydrology, 2015. **520**: p. 300-313.

539   50.   Cui, J., et al., *Global water availability boosted by vegetation-driven changes in atmospheric moisture*
540   *transport.* Nature Geoscience, 2022. **15**(12): p. 982-988.

541   51.   Souza, R., et al., *Vegetation response to rainfall seasonality and interannual variability in tropical dry*
542   *forests.* Hydrological Processes, 2016. **30**(20): p. 3583-3595.

543   52.   Kinzig, A.P., et al., *Resilience and regime shifts: assessing cascading effects.* Ecology and society, 2006.
544   **11**(1).

545   53.   Siqueira, M., G. Katul, and A. Porporato, *Onset of water stress, hysteresis in plant conductance, and*
546   *hydraulic lift: Scaling soil water dynamics from millimeters to meters.* Water Resources Research, 2008.
547   **44**(1).

548   54.   Zhang, G., et al., *Responses of grassland vegetation to climatic variations on different temporal scales in*
549   *Hulun Buir Grassland in the past 30 years.* Journal of Geographical Sciences, 2011. **21**: p. 634-650.

550   55.   Stillman, J.H., *Acclimation capacity underlies susceptibility to climate change.* Science, 2003. **301**(5629):
551   p. 65-65.

552   56.   Walters, R.G., *Towards an understanding of photosynthetic acclimation.* Journal of experimental botany,
553   2005. **56**(411): p. 435-447.

554   57.   Mengoli, G., et al., *Ecosystem photosynthesis in land surface models: a first principles approach*
555   *incorporating acclimation.* Journal of Advances in Modeling Earth Systems, 2022. **14**(1): p.
556   e2021MS002767.

Acknowledgement